Predicting Cerebral and Cardiovascular Variability from Wearable Biometrics

by

Chen Li

A thesis submitted to the
Department of Computer Science
in conformity with the requirements for
the degree of Master of Science

Bishop's University
Canada
September 2023

Abstract

Long-term, continuous monitoring of the human physiological state on a massive scale in the general population has the potential to revolutionize healthcare by detecting brain and cardiac disorders before they become life-threatening. Until recently, the technology for such monitoring has been lacking. Here, we present the first study examining the association between heart rate variability monitored through consumer-grade smartwatches and neuroanatomical metrics derived from high-resolution Magnetic Resonance Imaging (MRI) scans. Twenty-two subjects wore the watch for 1 month, continuously recording their heart rate through photoplethysmography (PPG), and then underwent a 1-hour MRI scan of the heart and brain. We found that several features of the heart rate waveform can predict blood flow velocity through the carotid and aorta arteries. Heart rate in beats per minute was positively associated with blood flow velocity through the aorta, and heart rate variability was inversely associated with blood flow velocity through both carotid arteries and aorta. We also performed full-brain correlations, finding, in general, that blood flow in the brain's gray matter was inversely correlated with HRV, carotid velocity, and some pulse-wave metrics. We consider this the first evidence that heart rate variability derived from consumer-grade smartwatch recordings can predict an individual's neuroanatomical features, such as blood flow in the cerebral arteries and gray matter, across a healthy population.

Acknowledgments

I would like to express my gratitude to Dr. Russell Butler and extend my heartfelt thanks to you for your invaluable guidance and support throughout the entire research process. Your expertise, passion, and patience have been instrumental in my progress in the field of study.

I am also writing to express my heartfelt gratitude for being selected as a recipient of the Graduate Entrance Scholarship at Bishop's University. It is with great honor and appreciation that I accept this generous scholarship, which has significantly lightened the financial burden of pursuing my academic goals. Receiving this scholarship not only provides me with financial assistance but also serves as a tremendous source of motivation and recognition for my hard work and dedication to my studies. It reaffirms my commitment to excel academically and reinforces my belief that hard work and perseverance can lead to rewarding opportunities.

Contents

1 Introduction **1**
- 1.1 Early warning signs . . . 1
- 1.2 Heart rate variability . . . 3
- 1.3 Previous studies using smartwatch . . . 4

2 Materials and methods **5**
- 2.1 Smartwatch hardware . . . 5
- 2.2 MRI scanner and sequences . . . 5
  - 2.2.1 T1-weighted image . . . 5
  - 2.2.2 Functional magnetic resonance imaging (fMRI) . . . 6
  - 2.2.3 Quantitative Flow (QFlow) . . . 7
- 2.3 Subjects . . . 9
- 2.4 Feature extraction: PPG . . . 10
  - 2.4.1 PPG waveform features . . . 10
  - 2.4.2 PPG feature extraction methods . . . 12
- 2.5 Feature extraction: MRI . . . 14
  - 2.5.1 Blood flow velocity calculation on the carotid arteries and the aorta . . . 14
  - 2.5.2 fMRI preprocessing and ReHo calculation . . . 15

3 Results **16**
- 3.1 PPG feature results . . . 16
  - 3.1.1 Time of day average BPM and accelerometer . . . 16
  - 3.1.2 The grand mean of BPM and accelerometer . . . 17
- 3.2 MRI feature results . . . 17
  - 3.2.1 Carotid artery waveforms and aorta waveforms for all subjects 17
  - 3.2.2 The grand mean of carotid artery waveforms and aorta waveforms . . . 18
  - 3.2.3 ReHo maps for all subjects and the grand mean of ReHo maps 19
- 3.3 Correlation results . . . 20
  - 3.3.1 Correlation matrix . . . 20
  - 3.3.2 Scatter plots . . . 21

3.4 ReHo correlation maps 22

4 Discussion **30**

Bibliography **31**

List of Tables

2.1 Samsung Galaxy Watch Active 2 Specifications 5
2.2 T1 Attributes 6
2.3 fMRI Attributes 7
2.4 QFlow (Carotid Artery) Attributes 8
2.5 QFlow (Aorta) Attributes 9

List of Figures

2.1 T1-weighted image. 6
2.2 BOLD fMRI image. 7
2.3 QFlow image of the carotid arteries. 8
2.4 QFlow image of the aorta. 9
2.5 Principle of phototoplethysmogram generation and waveform features. 11
2.6 Systolic peak, dicrotic notch, diastolic peak, and pulse width. 12
2.7 Crest time and peak to peak time. 12
2.8 A1 and A2. 12
2.9 Reflection index. 12
2.10 Raw PPG signal and filtered PPG signal. 13
2.11 The second derivative of photoplethysmography. (a) Fingertip photoplethysmogram. (b) Second derivative wave of photoplethysmogram. The photoplethysmogram waveform consists of one systolic wave and one diastolic wave, while the second derivative photoplethysmogram waveform consists of four systolic waves (a, b, c, and d waves) and one diastolic wave (e wave). 13
2.12 ROI on the carotid arteries. 14
2.13 ROI on the aorta. 14
2.14 Time series across carotid arteries. 14
2.15 Time series across aorta. 15
2.16 3D ReHo map. 15

3.1 Time of day average BPM and ACC. 16
3.2 The grand mean of BPM and ACC. 17
3.3 Carotid artery waveforms for all subjects. 17
3.4 Aorta waveforms for all subjects. 18
3.5 The grand mean of carotid artery waveforms. 18
3.6 The grand mean of aorta waveforms. 19
3.7 ReHo maps for all subjects. 19
3.8 The grand mean of ReHo. 20
3.9 Correlation matrix of all features. 20

3.10 Correlations between pulse-wave metrics and blood flow velocity metrics. . . . 21
3.11 Correlations between HRV and BPM metrics and blood flow velocity metrics. . . . 21
3.12 Correlation maps with BPM. . . . 22
3.13 Correlation maps with BPM (1AM to 6AM). . . . 23
3.14 Correlation maps with HRV. . . . 23
3.15 Correlation maps with HRV (1AM to 6AM). . . . 24
3.16 Correlation maps with age. . . . 24
3.17 Correlation maps with weight. . . . 25
3.18 Correlation maps with PW. . . . 25
3.19 Correlation maps with CT. . . . 26
3.20 Correlation maps with A1. . . . 26
3.21 Correlation maps with A2. . . . 27
3.22 Correlation maps with IPA. . . . 27
3.23 Correlation maps with PPT. . . . 28
3.24 Correlation maps with RI. . . . 28
3.25 Correlation maps with carotid blood flow velocity. . . . 29
3.26 Correlation maps with aorta blood flow velocity. . . . 29

Chapter 1

Introduction

1.1 Early warning signs

Alzheimer's disease (AD) is a progressive neurodegenerative disorder associated with significant financial expenses and caregiving burden [1]. The manifestation of AD covers a spectrum that extends from individuals without apparent symptoms but with pathological evidence of AD (referred to as preclinical AD) [2] to patients experiencing mild cognitive impairment (MCI) caused by AD (the initial clinically detectable stage of the disease) and eventually to those with AD dementia [3]. The characteristic pathological features of AD, namely β-amyloid plaques and neurofibrillary tangles, may be observable in the brain decades before clinical symptoms become evident [3]. Many individuals with early-stage AD remain undiagnosed, as subtle cognitive impairments may not significantly affect their daily activities. Such minor changes might be interpreted as normal signs of aging by patients, families, and healthcare providers (HCPs) [4]. As the disease progresses into AD dementia, symptoms of cognitive decline become more noticeable, frequently disrupting daily activities, and may prompt patients to seek medical attention [5].

Sleep disruption is a prevalent and often highly disruptive behavioral symptom associated with AD. It has been documented that Aβ deposition pathology itself can impact sleep architecture [6]. Zhang et al. have recently published new findings that shed light on this issue: they observed that sleep disturbance occurs prior to cognitive decline and even precedes the pre-pathological stage of AD [7]. Several animal studies have reported disturbances in sleep architecture and EEG at the pathological stage of AD [8,9]. Consistent with these animal findings, monitoring of patients with mild cognitive impairment (MCI) or mild-to-moderate AD has revealed changes in sleep EEG [10, 11]. Patients with mild-to-moderate AD exhibit abnormal theta oscillations in both rapid eye movement (REM) and slow-wave sleep [11]. Another study quantified the EEG during REM sleep in MCI patients and found EEG slowing in fronto-lateral regions compared to controls [10].

Zhang et al.'s research provides evidence that sleep disturbance already occurs before cognitive decline and even before the pre-pathological stage of AD [7]. These findings strongly suggest that changes in sleep EEG may serve as an early indicator of AD in the preclinical stage, offering valuable insights for preclinical evaluation and therapeutic intervention to prevent progression to symptomatic AD.

Moreover, cardiovascular disease (CVD) is increasingly recognized as an important etiological factor of AD. CVDs such as stroke, atrial fibrillation, coronary heart disease (CHD), and heart failure are highly prevalent in elderly individuals and have been consistently linked to AD. This association may arise from shared risk factors between CVDs and AD, but there could also be a direct causal relationship, as cardiac disease can lead to hypoperfusion and microemboli, which have been implicated in the etiology of AD [12, 13].

Early and accurate diagnosis of AD is crucial for prognosis and advance care planning [1]. While there is currently no approved treatment for the early stages of AD that can delay disease progression, a timely AD diagnosis allows for the initiation of advance care planning and non-pharmacological interventions. These interventions, such as cognitive stimulation, psychological treatment, and lifestyle changes, may help preserve cognitive function and improve the quality of life [14–17]. Additionally, lifestyle modifications and increased social support can alleviate caregiver burden, delay institutionalization, and reduce healthcare costs [18]. Overall, an early and accurate diagnosis facilitates the development of an effective care plan, which requires collaboration among patients, caregivers, family members, healthcare providers (HCPs), specialists, social services, and payers [5].

For individuals in the United States born in and before 2018, early and accurate diagnosis of AD could lead to cumulative savings of approximately $7 trillion in medical and care costs [1]. Despite the growing evidence supporting the benefits of early detection [18–20], and studies indicating that most patients and caregivers prefer disclosure of an AD diagnosis [21], the current diagnostic process for the early stages of AD needs improvement [22]. Although the recent US Preventive Services Task Force Recommendation Statement has raised concerns about insufficient evidence to weigh the benefits and risks of screening for cognitive impairment in older adults [23], experts have pointed out the current value of screening for mild cognitive impairment (MCI) and emphasized that the approval of therapies targeting the underlying pathophysiology of AD would further enhance the benefits of early screening [6].

By 2030, it is estimated that around 82 million people worldwide will have dementia, resulting in an annual cost of $2 trillion. Among these cases, 60 to 80% are likely to be attributed to AD [1]. To effectively screen and manage this increasing population of potential patients, additional resources are required. Currently, individuals suspected of having AD may face prolonged waiting periods for diagnosis or treatment, entangling them in a cycle of continuous referrals [4]. In the absence of an early-detection paradigm, the already limited healthcare infrastructure will

face additional strain when a therapy targeting the underlying pathophysiology of AD is eventually approved, leading to a surge of patients seeking treatment [22].

1.2 Heart rate variability

Heart rate refers to the number of heartbeats per minute, while heart rate variability (HRV) pertains to the variation in the time intervals between adjacent heartbeats [24]. HRV serves as an index of neurocardiac function and is influenced by interactions between the heart and brain, as well as dynamic non-linear processes within the autonomic nervous system (ANS). It is an emergent property of interconnected regulatory systems that adapt to environmental and psychological challenges on different time scales. HRV reflects the regulation of autonomic balance, blood pressure (BP), gas exchange, gut, heart, vascular tone (which regulates BP), and possibly facial muscles [25].

HRV can potentially indicate imbalances in the autonomic nervous system in a noninvasive manner. Data from numerous individuals show that lower HRV often corresponds to a fight-or-flight response, while higher HRV may indicate a more relaxed state. High HRV is associated with better cardiovascular fitness and greater resilience to stress. Additionally, HRV can provide personalized feedback on lifestyle choices, motivating individuals to adopt healthier habits such as mindfulness, meditation, sleep, and physical activity. By tracking HRV, individuals can observe how their nervous system responds not only to the environment but also to emotions, thoughts, and feelings [26].

Reduced HRV indices suggest diminished vagal activity and could potentially be linked to the onset of dementia. The progression of neurodegeneration is intertwined with cardiovascular autonomic regulation. In the systematic review conducted by da Silva et al. [27], the investigation focused on evaluating the effect size (ES) of HRV indexes as a method for assessing autonomic dysfunction in older individuals with dementia. The study aimed to explore the potential association between decreased HRV indexes, indicating reduced vagal activity, and the onset of dementia. This analysis considered the relationship between neurodegenerative processes and the control of cardiovascular autonomic functions. The findings of the study indicated that across various types of dementia and cases of mild cognitive impairment, the majority of HRV indexes demonstrated a negative effect size, suggesting impaired autonomic function. Notably, the high frequency range emerged as the predominant frequency band within the power spectrum density function, a pattern reported by six of the studies included in the review. However, the meta-analysis specifically focusing on high frequency power among individuals with Alzheimer's disease exhibited considerable heterogeneity and inconclusive results. The consistent negative effect size observed across different forms of dementia and mild cognitive impairment implies the presence of autonomic dysfunction. Nonetheless, the authors highlighted the need for further investigation

and rigorous analysis to establish robust support for these findings.

CVD is a leading cause of morbidity and mortality in developed nations. Non-invasive measurement of HRV is used to assess cardiac autonomic dysfunction, which is a risk factor for developing CVD [28]. Physiologically, HRV is believed to result from adaptive changes in heart rate driven by the sympathetic and parasympathetic nervous systems, aiming to regulate blood pressure [29]. Reduced compensatory changes (low HRV) suggest a weakened adaptive autonomic nervous system and are associated with increased morbidity. HRV has been linked to morbidity and mortality after myocardial infarction, as confirmed by multiple studies [30–32]. Furthermore, reduced HRV has been associated with congestive heart failure and arrhythmias [33, 34].

1.3 Previous studies using smartwatch

The prevalence of wearable medical technology has been steadily increasing every year [35]. Among consumers, the smartwatch has emerged as the most popular choice. These watches utilize photoplethysmographic signals to non-invasively monitor both heart rate and rhythm. Numerous studies have demonstrated the accurate monitoring of heart rhythms by smartwatches. For instance, the WATCH-AF trial demonstrated that photoplethysmographic-based smartwatches can accurately diagnose atrial fibrillation in 96% of cases compared to a diagnosis made by a cardiologist [36]. However, the trial also noted a high rate of subject dropout due to insignificant signal quality. While there have been emerging case reports of smartwatches detecting other types of atrial and ventricular tachycardias [37, 38], no reported cases of smartwatches leading to the incidental discovery of non-cardiovascular pathologies have been documented.

Clinicians should exercise caution and not fully rely on a device produced outside the rigorous healthcare standards. Perez et al. conducted a study involving nearly 420,000 patients who wore smartwatches for a median follow-up period of 117 days. Among them, 2,161 patients received alerts for an irregular heart rhythm, but only 450 returned ECG traces that could be analyzed. Ultimately, only 153 of these patients were confirmed to have an arrhythmia [39].

The purpose of this research is to investigate the potential of a consumer-grade wearable device to predict features of an individual's high-resolution anatomical MRI scan. This endeavor will establish the groundwork for a new era of wearable-derived biomarker extraction in preventive medicine. The ultimate objective, projected to be realized in the next 10+ years, is to leverage these consumer-grade wearable devices to provide early warning signs of potential failures in cardiac and cerebral systems.

Chapter 2

Materials and methods

2.1 Smartwatch hardware

To verify data quality from the Galaxy Watch, we conducted a pilot experiment involving simultaneous PPG recordings. These recordings were taken for 1 minute every 5 minutes throughout the duration of a single night on a single subject. After 30 days, the smartwatch was returned to the researcher, and the data were extracted.

Table 2.1 shows the hardware specifications for the device used in the experiment.

Table 2.1: Samsung Galaxy Watch Active 2 Specifications

Processor	Samsung Exynos 9110
RAM	750 MB
Storage	4 GB
Battery	340 mAh
Display	Super AMOLED, 360 x 360 Pixels
Camera	No
OS	Tizen-based wearable OS 4.0

2.2 MRI scanner and sequences

2.2.1 T1-weighted image

Figure 2.1 shows an axial slice from a representative subject's T1-weighted image.

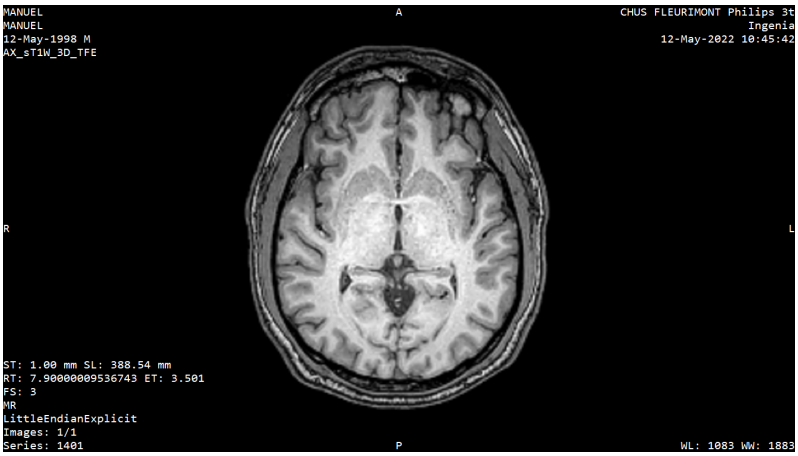

Figure 2.1: T1-weighted image.

Table 2.2 gives the MRI parameters used for the acquisition of the T1-weighted image.

Table 2.2: T1 Attributes

Manufacturer	Philips Medical Systems
Institution Name	CHUS FLEURIMONT Philips 3t
Body Part Examined	BRAIN
Slice Thickness	1
Repetition Time	8.11559963226318
Echo Time	3.722
Magnetic Field Strength	3
Spacing Between Slices	1

2.2.2 Functional magnetic resonance imaging (fMRI)

Figure 2.2 shows an axial slice from a representative subject's blood oxygen level dependent (BOLD) fMRI image. The BOLD fMRI image has a lower resolution than the T1 due to the fact that BOLD fMRI acquisition consists of repeated scans over time in order to acquire a time series of brain activity in each voxel.

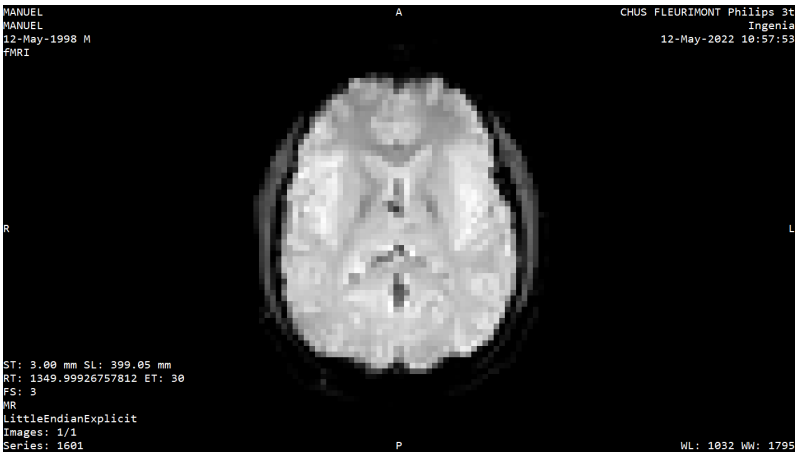

Figure 2.2: BOLD fMRI image.

Table 2.3 gives the MRI parameters used for the acquisition of the BOLD fMRI image.

Table 2.3: fMRI Attributes

Manufacturer	Philips Medical Systems
Institution Name	CHUS FLEURIMONT Philips 3t
Body Part Examined	BRAIN
Slice Thickness	3
Repetition Time	1349.99926757812
Echo Time	30
Magnetic Field Strength	3
Spacing Between Slices	3

2.2.3 Quantitative Flow (QFlow)

Figure 2.3 shows an axial slice from a representative subject's QFlow image of the carotid arteries.

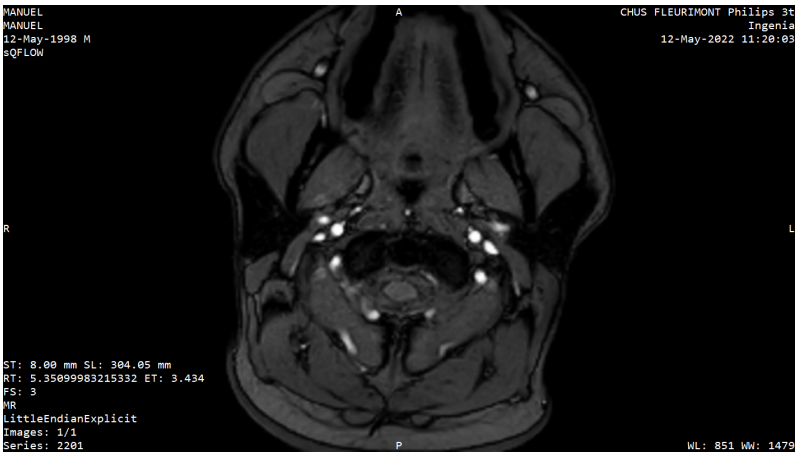

Figure 2.3: QFlow image of the carotid arteries.

Table 2.4 gives the MRI parameters used for the acquisition of the QFlow image of the carotid arteries.

Table 2.4: QFlow (Carotid Artery) Attributes

Manufacturer	Philips Medical Systems
Institution Name	CHUS FLEURIMONT Philips 3t
Body Part Examined	BRAIN
Slice Thickness	8
Repetition Time	5.42910003662109
Echo Time	3.474
Magnetic Field Strength	3
Spacing Between Slices	8

Figure 2.4 shows an axial slice from a representative subject's QFlow image of the aorta.

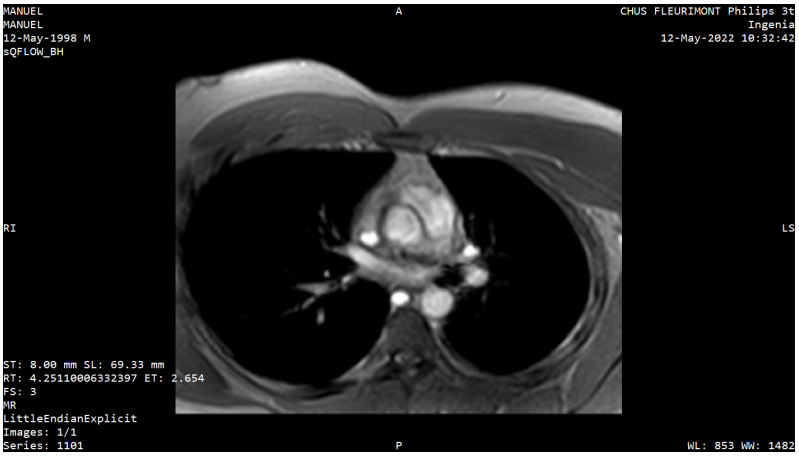

Figure 2.4: QFlow image of the aorta.

Table 2.5 gives the MRI parameters used for the acquisition of the QFlow image of the aorta.

Table 2.5: QFlow (Aorta) Attributes

Manufacturer	Philips Medical Systems
Institution Name	CHUS FLEURIMONT Philips 3t
Body Part Examined	HEART
Slice Thickness	8
Repetition Time	4.25110006332397
Echo Time	2.654
Magnetic Field Strength	3
Spacing Between Slices	8

2.3 Subjects

Twenty-two subjects were healthy 18-40 year old individuals, with a gender ratio of 1:1, selected from the local population of Sherbrooke, Quebec. All subjects were initially briefed on the nature of the study and the requirements throughout the study, including best practices for smartwatch usage (regularly charging the device, wearing it at night, etc.). Informed consent was obtained from all subjects prior to any data collection. Subjects wore the smartwatch for 1 month and then underwent a 1-hour MRI scan at the CHUS Fleurimont 3T Ingenia MRI scanner.

Subjects were compensated for their participation with a $150 CAD monetary reward.

2.4 Feature extraction: PPG

2.4.1 PPG waveform features

Figure 2.5 depicts the process of obtaining the PPG waveform, which is derived from the amount of light absorption recorded with a photodetector after light is transmitted through or reflected from human tissue [40]. The amplitude of the PPG waveform is measured in arbitrary units due to variations in physical characteristics among individuals, such as oxygen-carrying capacity, bone size, skin color, blood vessel distribution, cardiac output, vascular stiffness, and vascular compliance [41–43]. The measurement of the waveform is influenced by environmental factors, such as ambient light [44, 45].

The PPG waveform undergoes changes based on cardiac activity and can also be affected by respiration, autonomic nervous system activity, arterial activity, and venous activity [46–50]. Frequency analysis of the PPG waveform includes both cardiac and lung activities. Shin and Min have reported that most of the energy in the waveform is contained up to the 3rd harmonics [51]. The PPG waveform exhibits a rising curve during cardiac contraction (systolic phase) due to an increase in capillary blood volume and a descending curve during cardiac dilation (diastolic phase) caused by a decrease in capillary blood volume. The waveform repeats in response to cardiac activity. Pulse onset is defined as the point where pulsation begins, represented by the lowest blood volume before the systolic phase. The systolic peak is identified at the point of maximum blood volume. Transient rising and falling of the PPG waveform during diastole occur when blood volume in capillaries temporarily increases due to a pressure gradient in the opposite direction of blood flow, just before the aortic valve closes [52, 53]. At this moment, the recessed point is referred to as the dicrotic notch, and the point where the first derivative of the waveform is closest to zero after the systolic peak is known as the diastolic peak [54]. The PPG waveform can be influenced by body composition, physiological status, and external stimuli. Additionally, the PPG baseline is affected by factors like respiration, vascular compliance, vascular tone, pain, and drug use [55–57]. The amplitude of the systolic peak, a representative characteristic of the PPG waveform, is significantly correlated with microvascular expansion and is proportional to the cardiac output [58, 59]. The dicrotic notch is influenced by vascular tone and compliance, with its occurrence advancing with increased vascular tone [60]. Moreover, it has been observed that the time difference between the diastolic peak and systolic peak decreases with aging [61].

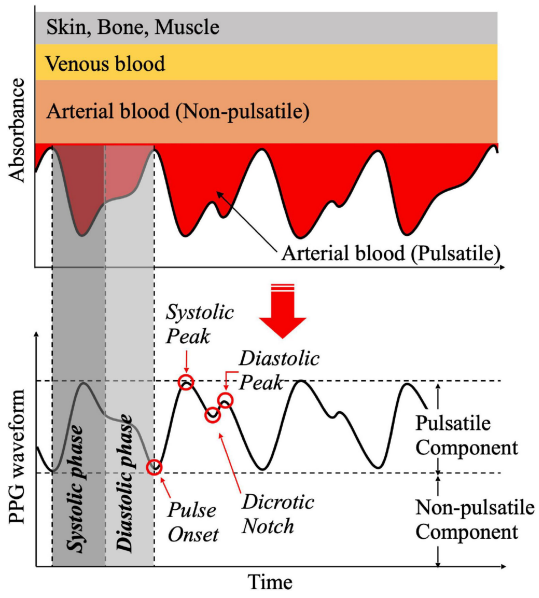

Figure 2.5: Principle of phototoplethysmogram generation and waveform features.

The PPG waveform has the following features:

- Beats per minute (BPM) is the number of times your heart beats per minute.
- Heart rate variability (HRV) is the physiological phenomenon of variation in the time interval between heartbeats.
- Systolic peak is defined at the point where blood volume is maximized [40].
- Dicrotic notch represents the closure of the aortic semi-lunar valve and subsequent receding blood flow when ventricles relax [40].
- Diastolic peak is a result of reflections of the pressure wave by arteries of the lower body [40].
- Pulse width (PW) is a measure of the elapsed time between the leading and trailing edges of a single pulse of energy [40].
- Crest time (CT) is the duration from the foot point to the peak of a pulse wave [40].
- Peak to peak time (PPT) is calculated as the time between the systolic and diastolic peaks within the PPG signal [40].
- A1 is the systolic area [62].
- A2 is the diastolic area [62].

- The inflection point area ratio (IPA) is used to refer to A2/A1 [62].
- Reflection index (RI) measures the stiffness level of small to moderate arteries [63].

Figures 2.6 to 2.9 show PPG waveform features computed in our method.

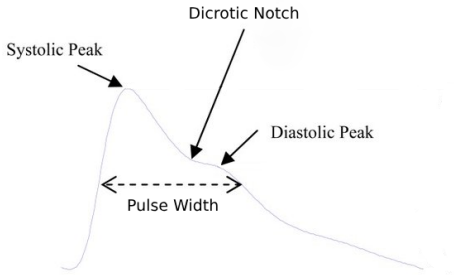

Figure 2.6: Systolic peak, dicrotic notch, diastolic peak, and pulse width.

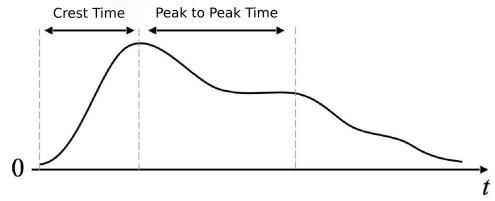

Figure 2.7: Crest time and peak to peak time.

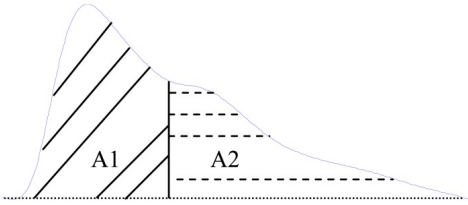

Figure 2.8: A1 and A2.

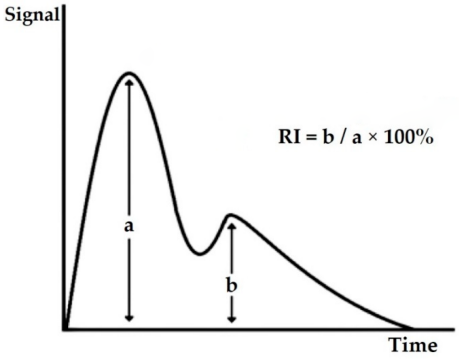

Figure 2.9: Reflection index.

2.4.2 PPG feature extraction methods

We create a script to process all CSV files, determining the most frequent BPM for each subject. Then, locate the corresponding CSV file based on the most frequent BPM. To mitigate the impact of baseline wander, apply a 5th-order Butterworth Infinite Impulse Response (IIR) high-pass filter with a cutoff frequency of 0.5 Hz to filter the PPG signal. Figure 2.10 shows a comparison before and after using the filter. To compute the PPG features for each subject, we use SciPy to calculate the troughs and peaks of each PPG waveform. The use of troughs also aims

to identify each individual PPG waveform within the PPG signal. Subsequently, we utilize the troughs, peaks, and the Second Derivative of Photoplethysmography (SDPPG) to compute the features for each individual waveform [64]. Figure 2.11 shows the Second Derivative of Photoplethysmography. Finally, we calculate the mean of these features. In certain instances, specific dicrotic notches and diastolic peaks might not be distinctly discernible. Therefore, exclude such instances to ensure the accuracy of the results.

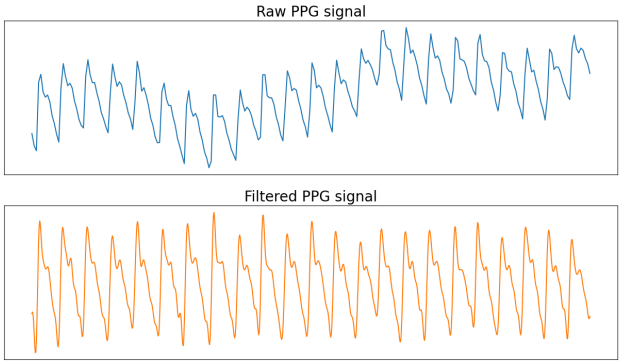

Figure 2.10: Raw PPG signal and filtered PPG signal.

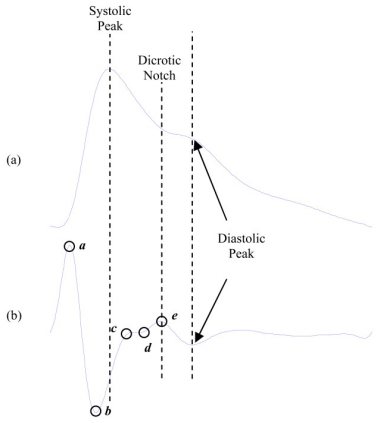

Figure 2.11: The second derivative of photoplethysmography. (a) Fingertip photoplethysmogram. (b) Second derivative wave of photoplethysmogram. The photoplethysmogram waveform consists of one systolic wave and one diastolic wave, while the second derivative photoplethysmogram waveform consists of four systolic waves (a, b, c, and d waves) and one diastolic wave (e wave).

2.5 Feature extraction: MRI

2.5.1 Blood flow velocity calculation on the carotid arteries and the aorta

We manually define a region of interest (ROI) mask on the qFLOW images. Figure 2.12 shows the ROIs of the left carotid artery and right carotid artery, and Figure 2.13 shows the ROI of the ascending aorta.

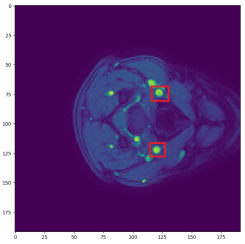

Figure 2.12: ROI on the carotid arteries.

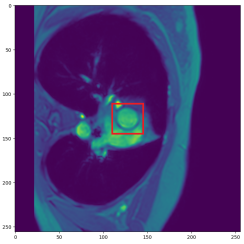

Figure 2.13: ROI on the aorta.

Then, we average the time series across all voxels in the mask and extract the velocity from the averaged time series across carotid arteries and aorta. Figures 2.14 and 2.15 show the velocity of a representative subject from the averaged time series across the carotid arteries and aorta, respectively.

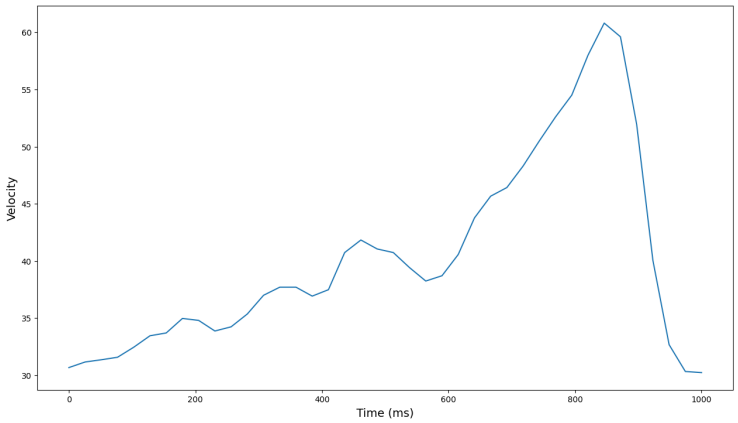

Figure 2.14: Time series across carotid arteries.

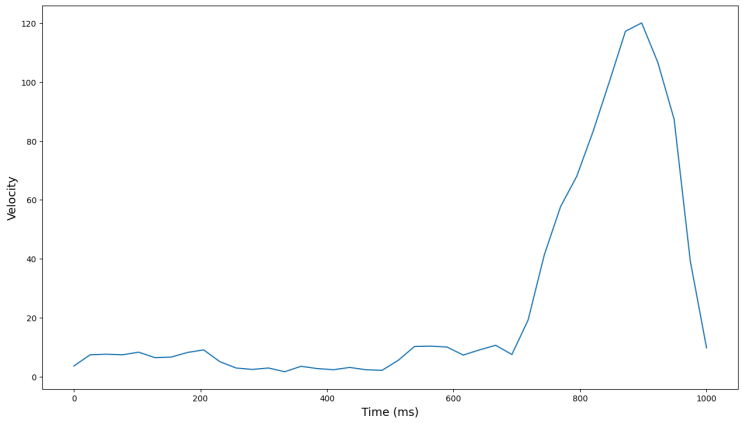

Figure 2.15: Time series across aorta.

2.5.2 fMRI preprocessing and ReHo calculation

The fMRI images underwent several preprocessing steps. Firstly, motion correction was applied, and then to account for small misalignments in the registration procedure, the images were smoothed with a 9 mm full-width half-maximum (FWHM) Gaussian kernel. A bandpass filter ranging from 0.01 to 0.1 Hz was subsequently applied to the data using the AFNI software package to remove physiological noise. After these steps, each fMRI image was registered to the space of a randomly selected template subject using the ANTs registration software package. Once aligned, regional homogeneity (ReHo) was calculated separately for each subject, resulting in a 3D ReHo map for each individual in template space. Figure 2.16 shows a representative subject's 3D ReHo map. These ReHo maps were then used in the subsequent full-brain correlation analysis.

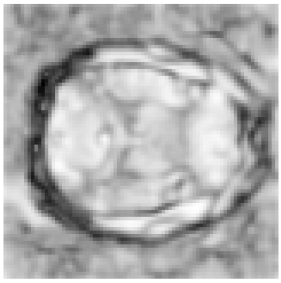

Figure 2.16: 3D ReHo map.

Chapter 3

Results

In this chapter, we present the PPG and MRI results of all subjects, and the means of all subjects (the grand mean).

3.1 PPG feature results

3.1.1 Time of day average BPM and accelerometer

Figure 3.1 shows the average heart rate in BPM and accelerometer (ACC) data extracted from the smartwatch and averaged over 30 days for a representative subject. The curve demonstrates a clear decrease in heart rate during the night (2 AM to 6 AM) during sleep, followed by an increase in heart rate and activity levels throughout the day.

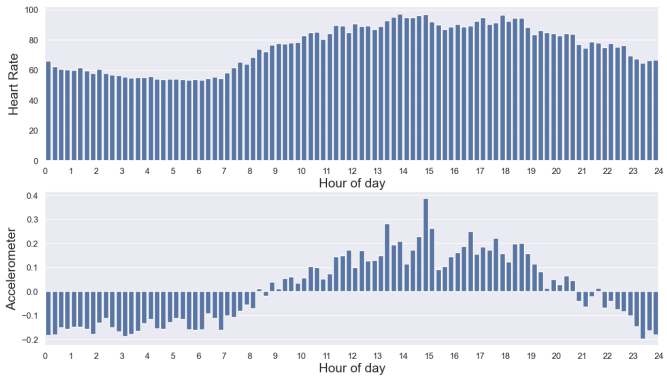

Figure 3.1: Time of day average BPM and ACC.

3.1.2 The grand mean of BPM and accelerometer

Figure 3.2 shows the grand mean of BPM and accelerometer.

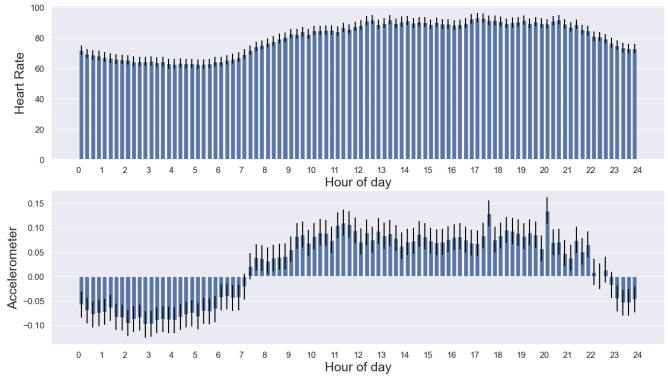

Figure 3.2: The grand mean of BPM and ACC.

3.2 MRI feature results

3.2.1 Carotid artery waveforms and aorta waveforms for all subjects

Figures 3.3 and 3.4 show the individual subject velocity waveform for carotid artery and aorta, respectively.

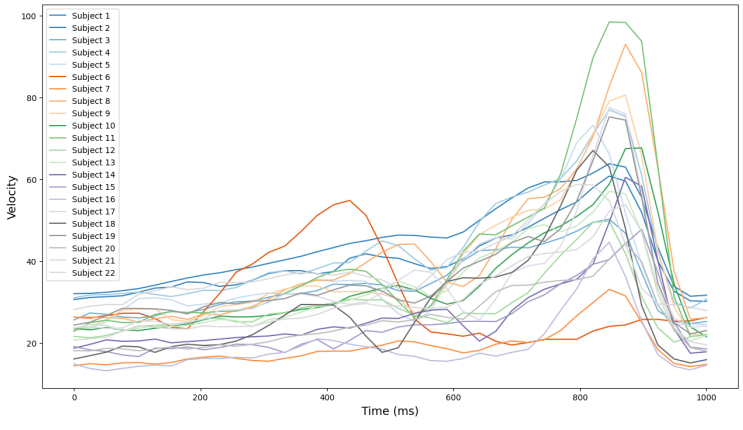

Figure 3.3: Carotid artery waveforms for all subjects.

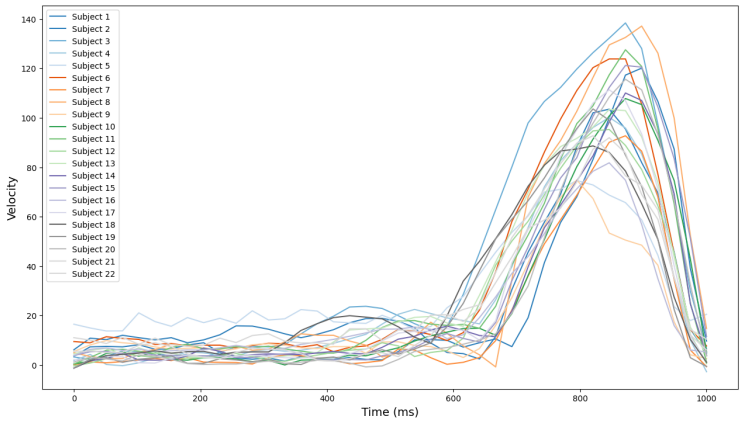

Figure 3.4: Aorta waveforms for all subjects.

3.2.2 The grand mean of carotid artery waveforms and aorta waveforms

Figures 3.5 and 3.6 show the grand mean across all subjects for carotid artery and aorta, respectively.

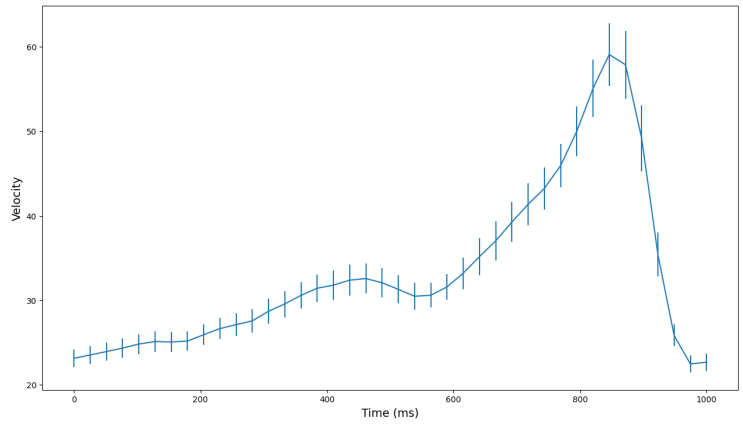

Figure 3.5: The grand mean of carotid artery waveforms.

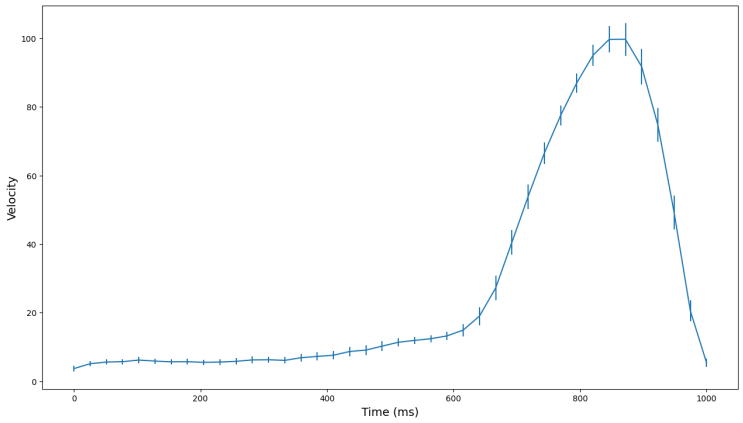

Figure 3.6: The grand mean of aorta waveforms.

3.2.3 ReHo maps for all subjects and the grand mean of ReHo maps

Figure 3.7 shows an axial slice in from each subject's raw ReHo map. As can be seen, ReHo values are higher in the gray matter.

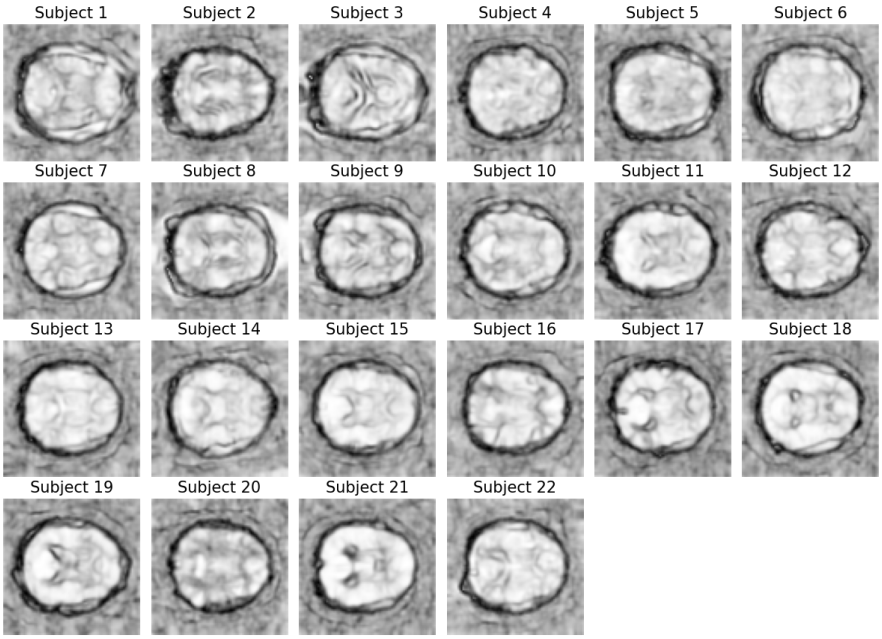

Figure 3.7: ReHo maps for all subjects.

Figure 3.8 shows the grand mean of ReHo map.

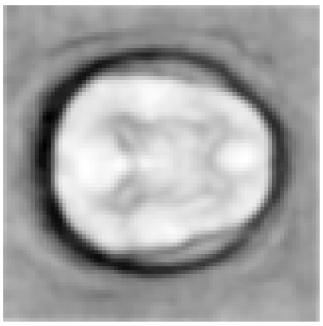

Figure 3.8: The grand mean of ReHo.

3.3 Correlation results

3.3.1 Correlation matrix

Figure 3.9 shows the correlation matrix between all features extracted from PPG and MRI.

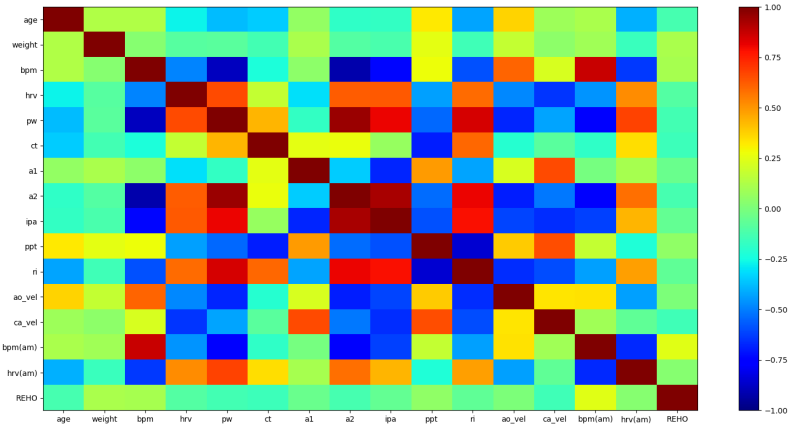

Figure 3.9: Correlation matrix of all features.

3.3.2 Scatter plots

Figure 3.10 shows the significant correlations found between PPG features and MRI velocity metrics from the carotid artery and aorta.

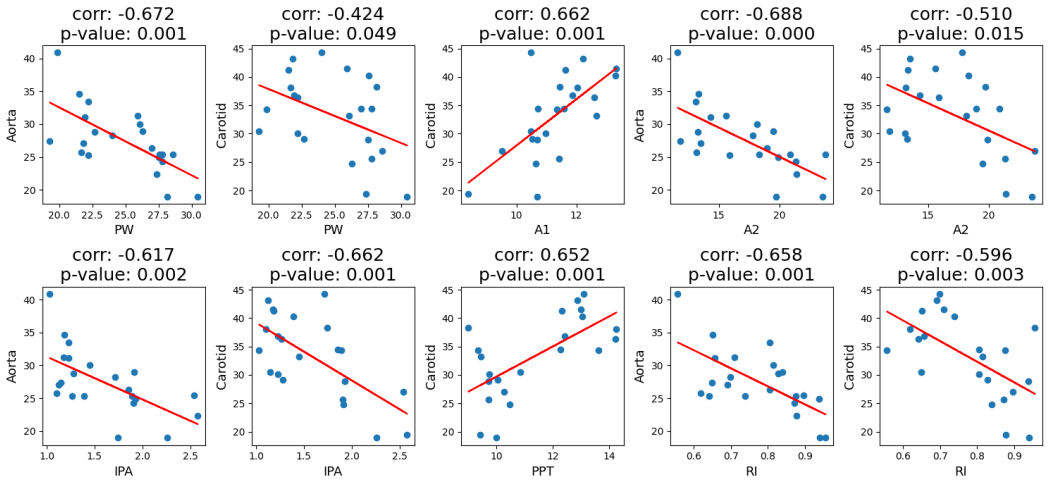

Figure 3.10: Correlations between pulse-wave metrics and blood flow velocity metrics.

Figure 3.11 shows the significant correlations between HRV and BPM metrics and velocity metrics. In general, subjects with higher HRV had lower arterial velocities, and subjects with higher heartrate had higher velocity.

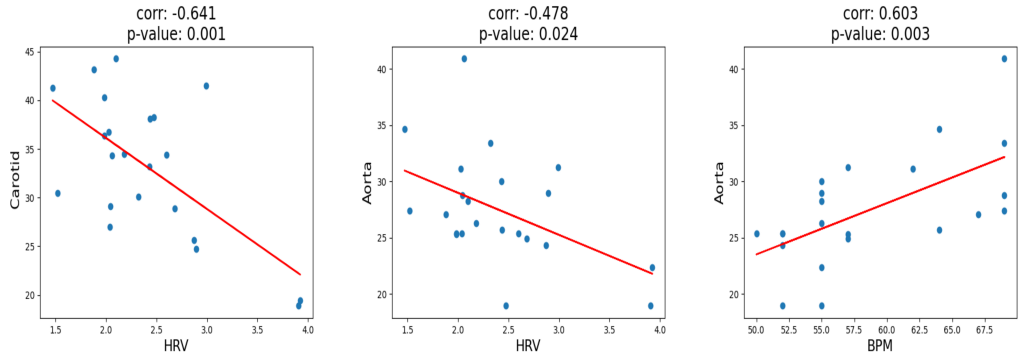

Figure 3.11: Correlations between HRV and BPM metrics and blood flow velocity metrics.

3.4 ReHo correlation maps

Sagittal slices showing full brain correlations between ReHo in each voxel and the PPG/velocity metrics are shown in Figures 3.12 to 3.26. Figure 3.12 (BPM), Figure 3.13 (BPM at night only), Figure 3.14 (HRV), Figure 3.15 (HRV at night only), Figure 3.16 (age), Figure 3.17 (weight), Figure 3.18 (PW), Figure 3.19 (CT), Figure 3.20 (A1), Figure 3.21 (A2), Figure 3.22 (IPA), Figure 3.23 (PPT), Figure 3.24 (RI), Figure 3.25 (velocity in carotid), Figure 3.26 (velocity in aorta). We found strong inverse correlations between HRV and ReHo in a voxel pattern matching the default-mode network (Figure 3.14) indicating that subjects with higher levels of HRV had lower glucose consumption in the default mode network. Weight was positively associated with ReHo across many voxels (Figure 3.17) indicating increased glucose consumption in heavier individuals. Figure 3.18 to 3.24 show correlations between metrics derived from PPG waveform and ReHo in each voxel. Most gray matter voxels show an inverse correlation, indicating that PPG waveform metrics are inversely correlated with glucose consumption across the brain. Finally, subjects with lower blood flow velocity through the carotid also had lower ReHo values in the gray matter (Figure 3.25), indicating that increased glucose consumption across the brain is associated with higher blood flow velocity.

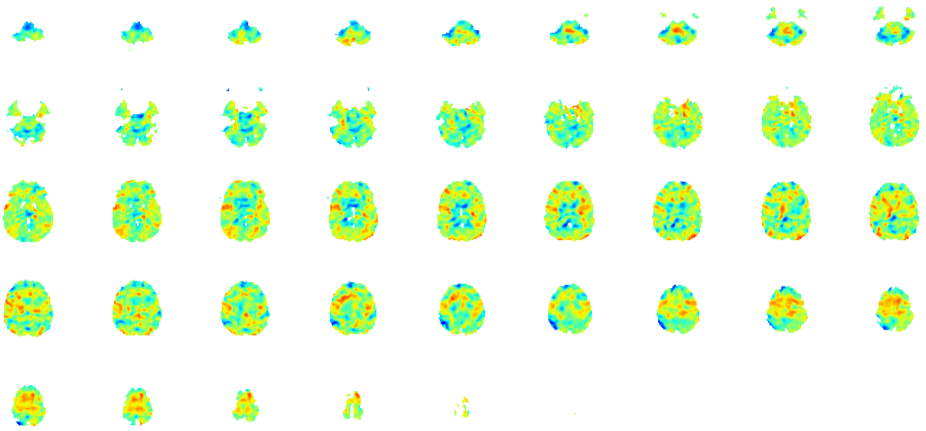

Figure 3.12: Correlation maps with BPM.

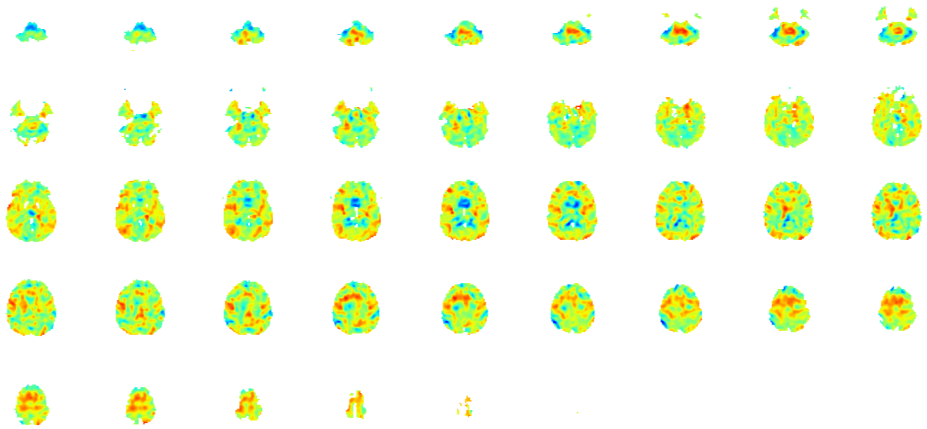

Figure 3.13: Correlation maps with BPM (1AM to 6AM).

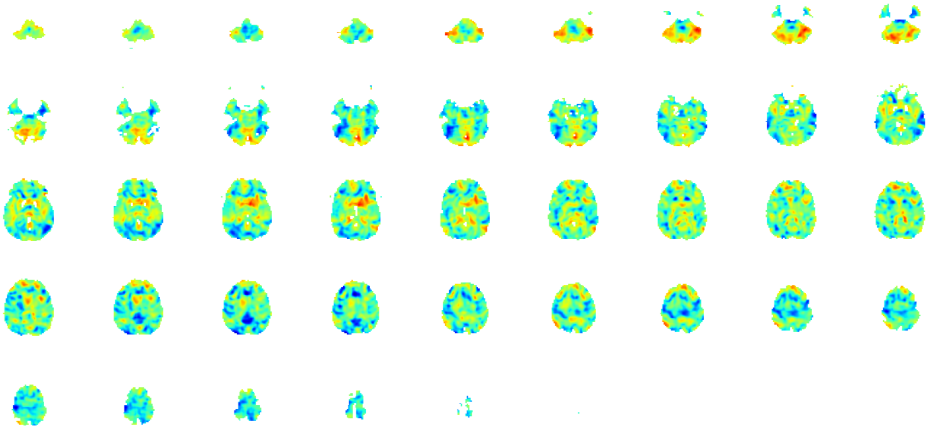

Figure 3.14: Correlation maps with HRV.

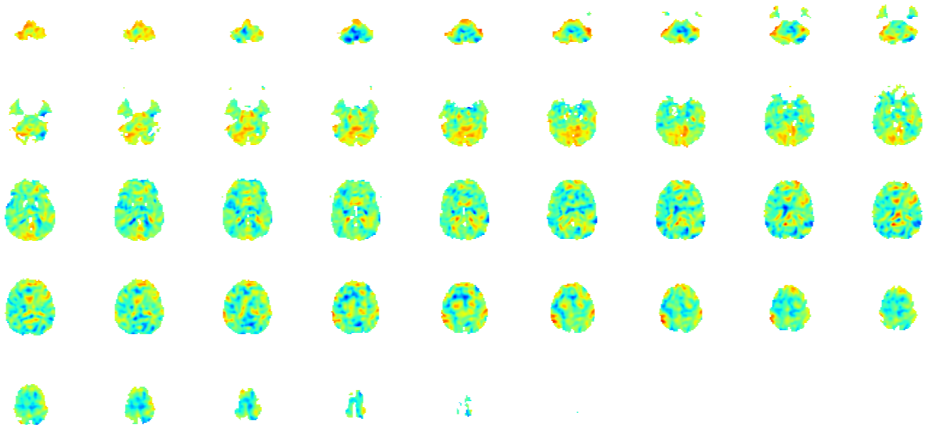

Figure 3.15: Correlation maps with HRV (1AM to 6AM).

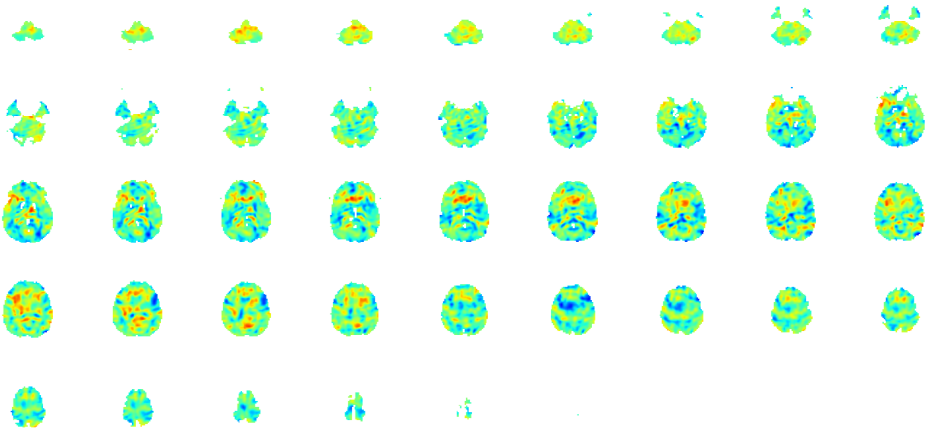

Figure 3.16: Correlation maps with age.

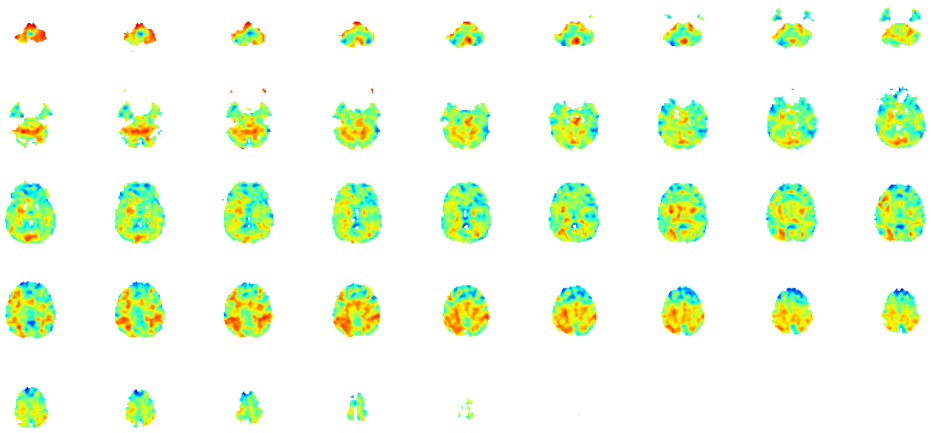

Figure 3.17: Correlation maps with weight.

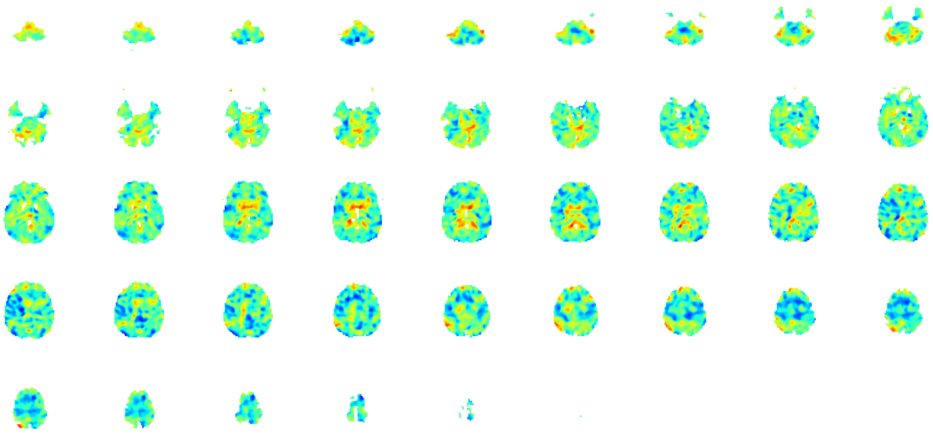

Figure 3.18: Correlation maps with PW.

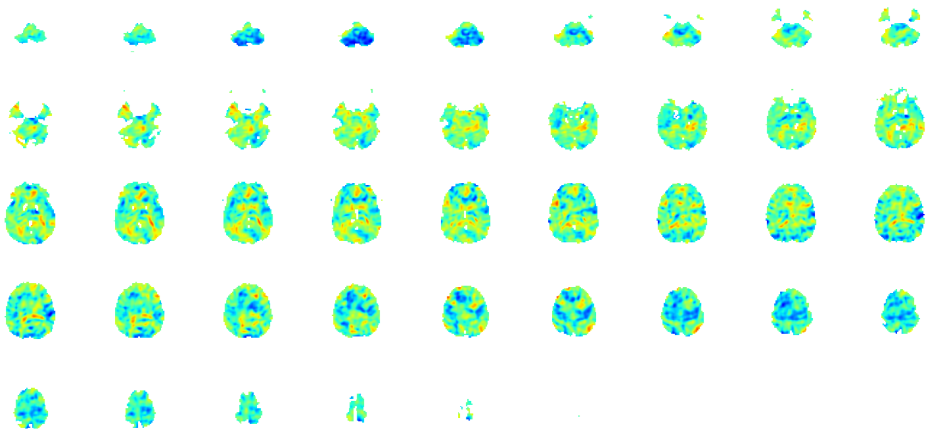

Figure 3.19: Correlation maps with CT.

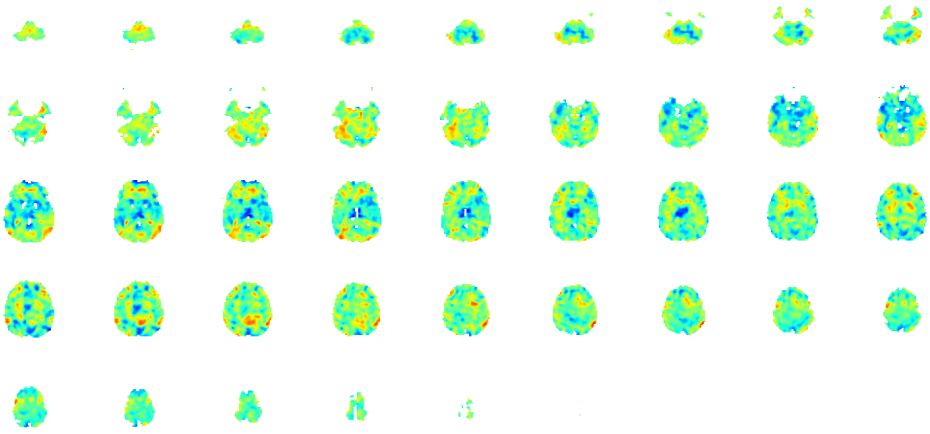

Figure 3.20: Correlation maps with A1.

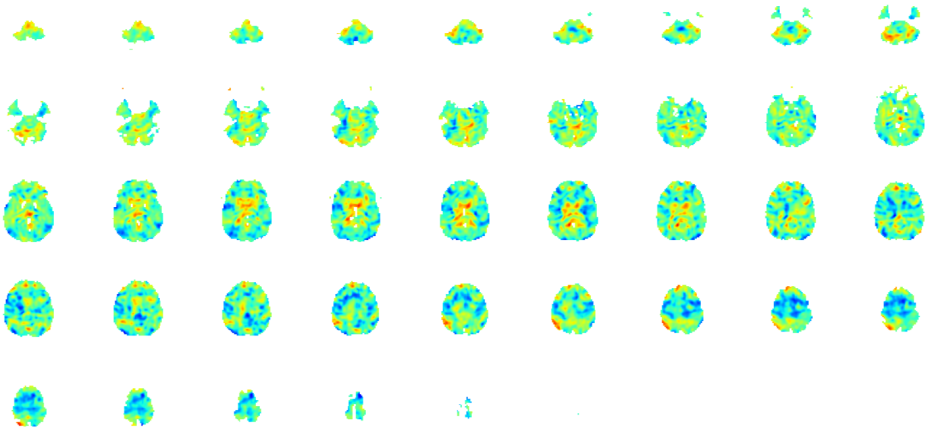

Figure 3.21: Correlation maps with A2.

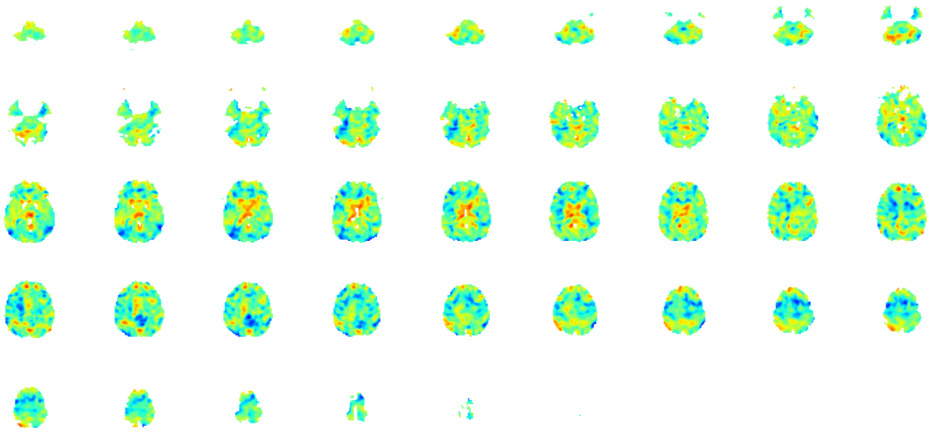

Figure 3.22: Correlation maps with IPA.

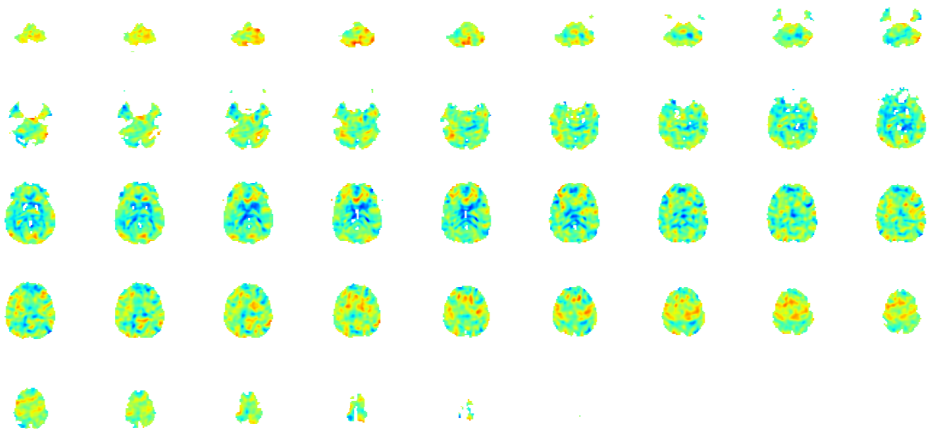

Figure 3.23: Correlation maps with PPT.

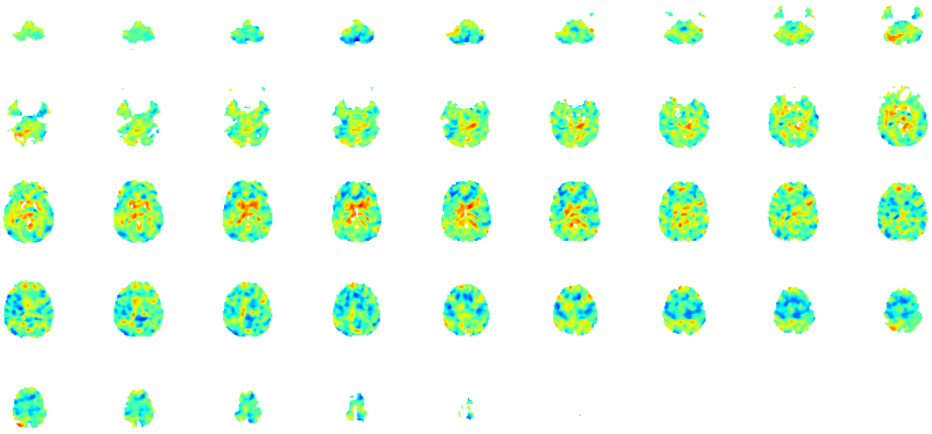

Figure 3.24: Correlation maps with RI.

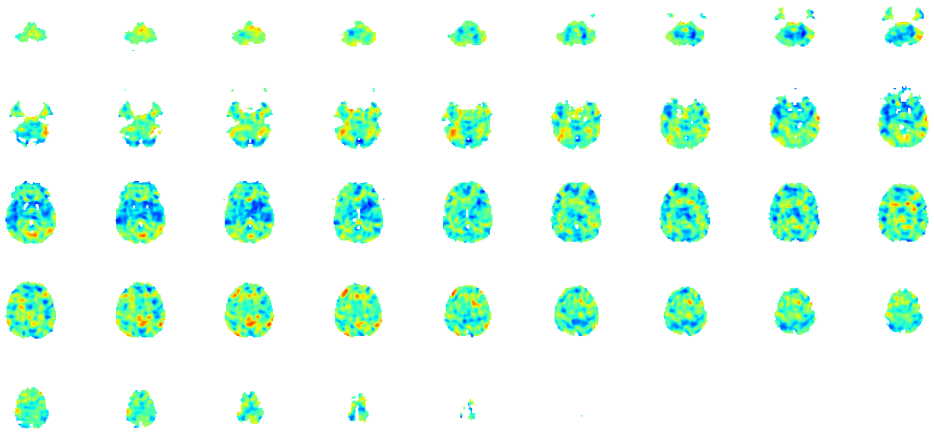

Figure 3.25: Correlation maps with carotid blood flow velocity.

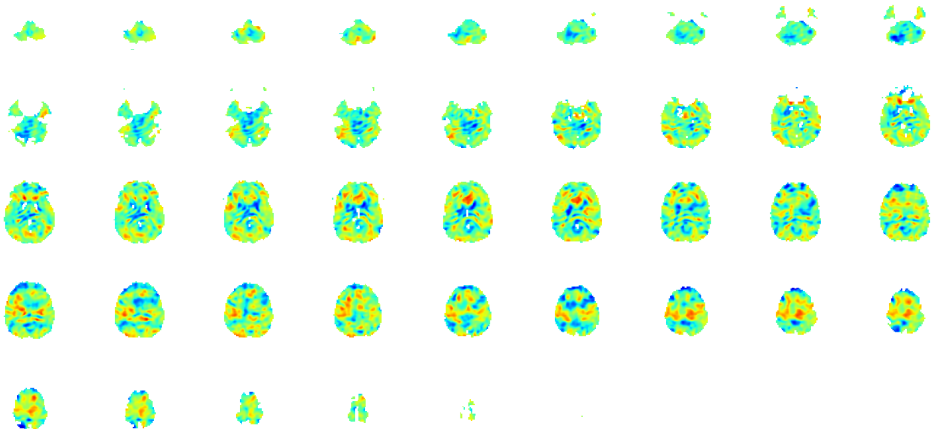

Figure 3.26: Correlation maps with aorta blood flow velocity.

Chapter 4

Discussion

We show results from the first study to investigate the association between heartrate metrics (HRV and others) derived from consumer-grade smartwatch and more sensitive metrics of cerebrovascular and cardiac function derived from detailed in-vivo MRI scans in a group of 22 healthy human subjects.

Our main results include the significant positive and negative correlations detected between several pulse-wave metrics (A1, A2, IPA, PPT, PW, RI) derived from the PPG signal and blood flow velocity through the carotid and aorta, as derived from the MRI scans. This indicates that within a healthy population, the velocity of an individual's blood flow can be predicted solely based on data acquired from a consumer-grade smartwatch device, which is a promising result. Additionally, we also found significant inverse correlations between HRV and carotid/aorta velocity. This is important because it has been well established that HRV is positively correlated with general metrics of well-being, including athletic performance, risk of heart attack, etc. The observed inverse correlation between HRV and higher blood flow velocity in the carotid/aorta suggests that elevated blood flow velocity may serve as an early risk factor for diseases such as stroke or heart attack.

Finally, we generated full-brain correlation maps between our PPG features and ReHo. ReHo is an fMRI-derived metric thought to serve as a proxy for glucose metabolism in the aging brain. Therefore, higher levels of ReHo are associated with higher levels of glucose metabolism. In general, we found inverse correlations between gray matter ReHo and both PPG and blood flow velocity metrics. The result, while awaiting further data to be confirmed, suggests that individuals with lower HRV may have 'less efficient' brains that require more glucose metabolism and a higher blood flow velocity to maintain basic cerebral function.

The future work will involve expanding the study to a cohort of healthy aging subjects (aged 65 and above) and to more specific populations, such as those suffering from dementia or those at a high risk of heart attack or stroke (including individuals who are overweight, diabetic, or have high blood pressure, etc.).

Bibliography

[1] Alzheimer's Association. Alzheimer's disease facts and figures. *Alzheimers Dement*, 16:391–460, 2020.

[2] Reisa A Sperling, Paul S Aisen, Laurel A Beckett, David A Bennett, Suzanne Craft, Anne M Fagan, et al. Toward defining the preclinical stages of alzheimer's disease: recommendations from the national institute on aging-alzheimer's association workgroups on diagnostic guidelines for alzheimer's disease. *Alzheimers Dement*, 7:280–292, 2011.

[3] Clifford R Jack Jr, David A Bennett, Kaj Blennow, Maria C Carrillo, Brooks Dunn, Samantha B Haeberlein, et al. Nia-aa research framework: toward a biological definition of alzheimer's disease. *Alzheimers Dement*, 14:535–562, 2018.

[4] Gerontological Society of America. The gerontological society of america workgroup on cognitive impairment detection and earlier diagnosis: Report and recommendations. 2015.

[5] Alzheimer's Association. Alzheimer's disease facts and figures. *Alzheimers Dement*, 15:321–387, 2019.

[6] Ronald C. Petersen and Kristine Yaffe. Issues and questions surrounding screening for cognitive impairment in older patients. *JAMA*, 323:722–724, 2020.

[7] Fang Zhang, Rong Zhong, Shanshan Li, Zhiqin Fu, Rong Wang, Tao Wang, and et al. Alteration in sleep architecture and electroencephalogram as an early sign of alzheimer's disease preceding the disease pathology and cognitive decline. *Alzheimers Dement*, 15:590–597, 2019.

[8] Amar Jyoti, Andrew Plano, Gernot Riedel, and Bettina Platt. Eeg, activity, and sleep architecture in a transgenic abetappswe/psen1a246e alzheimer's disease mouse. *J Alzheimers Dis*, 22:873–887, 2010.

[9] Florian Schneider, Kathrin Baldauf, Wiebke Wetzel, and Klaus G. Reymann. Behavioral and eeg changes in male 5xfad mice. *Physiol Behav*, 135:25–33, 2014.

[10] Pauline Brayet, David Petit, Birgit Frauscher, Jean-François Gagnon, Nadia Gosselin, Katia Gagnon, and et al. Quantitative eeg of rapid-eye-movement sleep: a marker of amnestic mild cognitive impairment. *Clin EEG Neurosci*, 47:134–141, 2016.

[11] Pascaline Hot, Gael Rauchs, Fanny Bertran, Pierre Denise, Béatrice Desgranges, Patrice Clochon, and et al. Changes in sleep theta rhythm are related to episodic memory impairment in early alzheimer's disease. *Biol Psychol*, 87:334–339, 2011.

[12] I. Goldberg, E. Auriel, D. Russell, and A. D. Korczyn. Microembolism, silent brain infarcts and dementia. *J Neurol Sci*, 322:250–253, 2012.

[13] J. C. de la Torre. Cardiovascular risk factors promote brain hypoperfusion leading to cognitive decline and dementia. *Cardiovasc Psychiatry Neurol*, 2012, 2012.

[14] Barbara G Vickrey, Brian S Mittman, Karen I Connor, Marjorie L Pearson, Richard D Della Penna, Theodore G Ganiats, and et al. The effect of a disease management intervention on quality and outcomes of dementia care: a randomized, controlled trial. *Annals of Internal Medicine*, 145:713–726, 2006.

[15] Naoko Kishita, Tamara Backhouse, and Eneida Mioshi. Nonpharmacological interventions to improve depression, anxiety, and quality of life (qol) in people with dementia: an overview of systematic reviews. *Journal of Geriatric Psychiatry and Neurology*, 33:28–41, 2020.

[16] Rodrigo L M Fukushima, Eduardo G do Carmo, Renato D V Pedroso, Paul N Micali, Patrícia S Donadelli, Guilherme J Fuzaro, and et al. Effects of cognitive stimulation on neuropsychiatric symptoms in elderly with alzheimer's disease: a systematic review. *Dementia & Neuropsychologia*, 10:178–184, 2016.

[17] C Groot, Astrid M Hooghiemstra, Pieter G Raijmakers, Bart NM van Berckel, Philip Scheltens, Erik J A Scherder, and et al. The effect of physical activity on cognitive function in patients with dementia: a meta-analysis of randomized control trials. *Ageing Research Reviews*, 25:13–23, 2016.

[18] Marta Crous-Bou, Carolina Minguillon, Nina Gramunt, and Jose Luis Molinuevo. Alzheimer's disease prevention: from risk factors to early intervention. *Alzheimer's Research & Therapy*, 9:71, 2017.

[19] Jonathan F Hodes, Christina I Oakley, James H O'Keefe, Peijun Lu, James E Galvin, Nader Saif, and et al. Alzheimer's "prevention" vs. "risk reduction": transcending semantics for clinical practice. *Front Neurol*, 9:1179, 2018.

[20] Gaurav Rakesh, Steven T Szabo, George S Alexopoulos, and Anthony S Zannas. Strategies for dementia prevention: latest evidence and implications. *Ther Adv Chronic Dis*, 8:121–136, 2017.

[21] Alzheimer's Association. 2015 alzheimer's disease facts and figures. *Alzheimers Dement*, 11:332–384, 2015.

[22] Jen-Hsiang Leslie Liu, Jillian P Hlavka, Roland Hernandez, and Soeren Mattke. Assessing the preparedness of the u.s. health care system infrastructure for an alzheimer's treatment. RAND Research Report, 2017.

[23] US Preventive Services Task Force, Douglas K. Owens, Karina W. Davidson, Alex H. Krist, Michael J. Barry, Michael Cabana, and et al. Screening for cognitive impairment in older adults: US Preventive Services Task Force recommendation statement. *JAMA*, 323:757–763, 2020.

[24] R. McCraty and F. Shaffer. Heart rate variability: new perspectives on physiological mechanisms, assessment of self-regulatory capacity, and health risk. *Glob Adv Health Med*, 4:46–61, 2015.

[25] R. N. Gevirtz, P. M. Lehrer, and M. S. Schwartz. Cardiorespiratory biofeedback. In M. S. Schwartz and F. Andrasik, editors, *Biofeedback: A Practitioner's Guide*, pages 196–213. The Guilford Press, New York, 2016.

[26] Harvard Health Publishing Staff. Heart rate variability: How it might indicate well-being. December 1 2021.

[27] Vanessa Silva, Bruno Oliveira, Roger Mello, Helena Moraes, Andréa Deslandes, and Jerson Laks. Heart rate variability indexes in dementia: A systematic review with a quantitative analysis. *Current Alzheimer Research*, 15(1):80–88, 05 2017.

[28] Task Force of the European Society of Cardiology and the North American Society of Pacing and Electrophysiology. Heart rate variability. standards of measurement, physiological interpretation, and clinical use. *Eur Heart J*, 17:354–381, 1996.

[29] S. Akselrod, D. Gordon, J. B. Madwed, N. C. Snidman, D. C. Shannon, and R. J. Cohen. Hemodynamic regulation: investigation by spectral analysis. *Am J Physiol*, 249:H867–H875, 1985.

[30] M. M. Wolf, G. A. Varigos, D. Hunt, and J. G. Sloman. Sinus arrhythmia in acute myocardial infarction. *Med J Aust*, 2:52–53, 1978.

[31] Maria Teresa La Rovere, J. T. Jr Bigger, F. I. Marcus, A. Mortara, and P. J. Schwartz. Baroreflex sensitivity and heart-rate variability in prediction of total cardiac mortality after myocardial infarction. *Lancet*, 351:478–484, 1998.

[32] J. T. Jr Bigger, J. L. Fleiss, R. C. Steinman, L. M. Rolnitzky, R. E. Kleiger, and J. N. Rottman. Frequency domain measures of heart period variability and mortality after myocardial infarction. *Circulation*, 85:164–171, 1992.

[33] Gavin R. Sandercock and David A. Brodie. The role of heart rate variability in prognosis for different modes of death in chronic heart failure. *Pacing Clin Electrophysiol*, 29:892–904, 2006.

[34] David Andresen and Thomas Bruggemann. Heart rate variability preceding onset of atrial fibrillation. *J Cardiovasc Electrophysiol*, 9:S26–S29, 1998.

[35] S. Mittal. Smartphone-based electrocardiographic and cardiac implantable electronic device monitoring. *Cardiol Rev*, 25:12–16, 2017.

[36] M. Dörr, V. Nohturfft, N. Brasier, and et al. The watch af trial: smartwatches for detection of atrial fibrillation. *JACC Clin Electrophysiol*, 5(2):199–208, 2019.

[37] L. N. Goldstein and M. Wells. Smart watch-detected tachycardia: a case of atrial flutter. *Oxf Med Case Reports*, 2019(12):495–497, 2019.

[38] M. Ringwald, A. Crich, and N. Beysard. Smart watch recording of ventricular tachycardia: case study. *Am J Emerg Med*, 2019.

[39] Marco V Perez, Kenneth W Mahaffey, Haley Hedlin, John S Rumsfeld, Alan Garcia, Timothy Ferris, Vidya Balasubramanian, Andrea M Russo, Arjun Rajmane, Lee Cheung, Grace Hung, Joseph Lee, Peter Kowey, Nisha Talati, Divya Nag, Sravya E Gummidipundi, Alexis Beatty, Michael T Hills, Sanjiv Desai, Christopher B Granger, Mehul Desai, and Mintu P Turakhia. Large-scale assessment of a smartwatch to identify atrial fibrillation. *New England Journal of Medicine*, 381(20), 11 2019.

[40] Junyung Park, Hyeon Seok Seok, Sang-Su Kim, and Hangsik Shin. Photoplethysmogram analysis and applications: An integrative review. *Frontiers in Physiology*, 12, 2022.

[41] Qingshan Zhang, Lars-Goran Lindberg, Roland Kadefors, and Jorma Styf. A non-invasive measure of changes in blood flow in the human anterior tibial muscle. *European Journal of Applied Physiology*, 84(5):448–452, 2001.

[42] Aravind Krishnaswamy and Gladimir V. Baranoski. A biophysically-based spectral model of light interaction with human skin. *Computer Graphics Forum*, 23(3):331–340, 2004.

[43] Tom Valencell. *Optical Heart Rate Monitoring: What You Need to Know*. Valencell, Raleigh, 2015.

[44] Xiaobai Li, Jiajiong Chen, Guoying Zhao, and Matti Pietikainen. Remote heart rate measurement from face videos under realistic situations. In *Proceedings of the IEEE Conference on Computer Vision and Pattern Recognition*, pages 4264–4271. IEEE, 2014.

[45] Li Xu, Jia Cheng, and Xiang Chen. Illumination variation interference suppression in remote ppg using pls and memd. *Electronics Letters*, 53(4):216–218, 2017.

[46] Neil D. McKay, Ben Griffiths, Cristina Di Maria, Suzanne Hedley, Andrew Murray, and John Allen. Novel photoplethysmography cardiovascular assessments in patients with raynaud's phenomenon and systemic sclerosis: a pilot study. *Rheumatology*, 53(10):1855–1863, 2014.

[47] Marco A. Pimentel, Peter H. Charlton, and David A. Clifton. Probabilistic estimation of respiratory rate from wearable sensors. In Subhas C. Mukhopadhyay, editor, *Wearable Electronics Sensors*, pages 241–262. Springer, Berlin, 2015.

[48] Matt Bentham, Gerard Stansby, and John Allen. Innovative multi-site photoplethysmography analysis for quantifying pulse amplitude and timing variability characteristics in peripheral arterial disease. *Diseases*, 6:81, 2018.

[49] Swathi Lakshmanan, Debatri Chatterjee, and Manikandan Muniyandi. Non-invasive assistive method to diagnose arterial disease-takayasu's arteritis. In D. J. Hemanth and S. Smys, editors, *Computational Vision and Bio Inspired Computing*, pages 384–398. Springer, Berlin, 2018.

[50] Hao Yuan, Shah Faisal Memon, Thomas Newe, Elfed Lewis, and Gabriel Leen. Motion artefact minimization from photoplethysmography based non-invasive hemoglobin sensor based on an envelope filtering algorithm. *Measurement*, 115:288–298, 2018.

[51] Hoon Shin and Se Dong Min. Feasibility study for the non-invasive blood pressure estimation based on ppg morphology: normotensive subject study. *Biomedical Engineering Online*, 16:10, 2017.

[52] Göran Dahlgren, Francisco Veintemilla, Georg Settergren, and Jan Liska. Left ventricular end-systolic pressure estimated from measurements in a peripheral artery. *Journal of Cardiothoracic and Vascular Anesthesia*, 5:551–553, 1991.

[53] Jia-Liang He, Yves Lecarpentier, Kambiz Zamani, Catherine Coirault, Ghassan Daccache, Denis Chemla, and Edmee Lecarpentier. Relation between aortic dicrotic notch pressure and mean aortic pressure in adults. *The American Journal of Cardiology*, 76:301–306, 1995.

[54] Sandrine C. Millasseau, Robert Kelly, James Ritter, and Philip Chowienczyk. Determination of age-related increases in large artery stiffness by digital pulse contour analysis. *Clinical Science*, 103:371–377, 2002.

[55] Meir Nitzan, Igal Faib, and Hadar Friedman. Respiration-induced changes in tissue blood volume distal to occluded artery, measured by photoplethysmography. *Journal of Biomedical Optics*, 11:040506, 2006.

[56] Kirk H. Shelley, David H. Jablonka, Ameen A. Awad, Robert G. Stout, Hani Rezkanna, and David G. Silverman. What is the best site for measuring the effect of ventilation on the pulse oximeter waveform? *Anesthesia & Analgesia*, 103:372–377, 2006.

[57] Kirk H. Shelley. Photoplethysmography: beyond the calculation of arterial oxygen saturation and heart rate. *Anesthesia & Analgesia*, 105:S31–S36, 2007.

[58] J. Dorlas and J. Nijboer. Photo-electric plethysmography as a monitoring device in anaesthesia: application and interpretation. *British Journal of Anaesthesia*, 57:524–530, 1985.

[59] W. B. Murray and P. A. Foster. The peripheral pulse wave: information overlooked. *Journal of Clinical Monitoring*, 12:365–377, 1996.

[60] P. Shi, S. Hu, Y. Zhu, J. Zheng, Y. Qiu, and P. Cheang. Insight into the dicrotic notch in photoplethysmographic pulses from the finger tip of young adults. *Journal of Medical Engineering & Technology*, 33:628–633, 2009.

[61] Q. Yousef, M. Reaz, and M. A. M. Ali. The analysis of ppg morphology: investigating the effects of aging on arterial compliance. *Measurement Science Review*, 12:266–271, 2012.

[62] Mohamed Elgendi. On the analysis of fingertip photoplethysmogram signals. *Current cardiology reviews*, 8:14–25, 02 2012.

[63] Paolo Salvi, Elena Magnani, Filippo Valbusa, Davide Agnoletti, Cosmin Alecu, Laurent Joly, and Athanase Benetos. Comparative study of methodologies for pulse wave velocity estimation. *Journal of Human Hypertension*, 22:669–677, 2008.

[64] Mohamed Elgendi, Ian Norton, Matt Brearley, Derek Abbott, and Dale Schuurmans. Detection of a and b waves in the acceleration photoplethysmogram. *BioMedical Engineering OnLine*, 13(1):139, 2014.